Emergence and detailed structure of terraced surfaces produced by oblique-incidence ion sputtering

Matt P. Harrison, Daniel A. Pearson, and R. Mark Bradley

Phys. Rev. E **96**, 032804 — Published 25 September 2017

DOI: 10.1103/PhysRevE.96.032804

Emergence and Detailed Structure of Terraced Surfaces Produced by Oblique-Incidence Ion Sputtering

Matt P. Harrison, Daniel A. Pearson, and R. Mark Bradley

Department of Physics, Colorado State University, Fort Collins, CO 80523, USA

Abstract

We study the nanoscale terraced topographies that arise when a solid surface is bombarded with a broad ion beam that has a relatively high angle of incidence θ. We find that the surface is not completely flat between the regions in which the surface slope changes rapidly with position: instead, small amplitude ripples propagate along the surface. Our analytical work on these ripples yields their propagation velocity as well as the scaling behavior of their amplitude. Our simulations establish that the surfaces exhibit interrupted coarsening, i.e., the characteristic width and height of the surface disturbance grow for a time but ultimately asymptote to finite values as the fully terraced state develops. In addition, as θ is reduced, the surface can undergo a transition from a terraced morphology that changes little with time as it propagates over the surface to an unterraced state that appears to exhibit spatiotemporal chaos. For different ranges of the parameters, our equation of motion produces unterraced topographies that are remarkably similar to those seen in various experiments, including pyramidal structures that are elongated along the projected beam direction and isolated lenticular depressions.

PACS numbers: 81.16.Rf, 79.20.Rf, 68.35.Ct

I. INTRODUCTION

When a nominally flat solid surface is bombarded with an obliquely-incident, broad ion beam, nanoscale ripples often develop on the surface [1]. These ripples form as a result of a surface instability [2–4]. At early times, the surface is governed by a linear equation of motion to a good approximation and the ripple amplitude grows exponentially in time. However, nonlinear effects must be taken into account once the ripple amplitude has become sufficiently large. The lowest order nonlinearities are quadratic and come from the angular dependence of the sputter yield [5, 6]. When these terms are included, the equation of motion for the surface becomes the anisotropic Kuramoto-Sivashinsky (KS) equation. This equation yields disordered ripples whose amplitude saturates at sufficiently long times.

In experiments in which the ion beam is reasonably close to grazing incidence, the surface frequently develops a terraced form at the late stages of its time evolution [7–20]. A height profile taken along the projected ion direction is not sinusoidal. Instead, as we trace along the profile, the surface slope is nearly equal to a constant positive value m_+ for a long spatial interval. At some point, the slope changes rapidly, and then is nearly equal to a constant negative value m_- for a long interval. The slope once again changes rapidly at some point, and then is approximately equal to m_+. The height profile continues in this fashion, and so takes on an irregular, sawtooth form. The sawteeth are asymmetric because the magnitudes of the selected slopes m_+ and m_- differ.

The anisotropic KS equation does not produce terraced topographies. However, Pearson and Bradley (PB) recently introduced a model that includes a better approximation to the sputter yield than the one that is used in deriving the KS equation [21]. This more refined approximation yields a cubic nonlinearity that does not appear in the KS equation. Numerical integrations of the PB equation of motion reveal that the cubic term can have a profound effect on the dynamics — it can lead to the formation of a terraced topography that coarsens with time, in accord with experimental observations [7–20]. The regions in which the surface slope changes rapidly are undercompressive shocks [22].

The formation of terraced surfaces is not just of academic interest. Harrison and Bradley (HB) have advanced a two-stage procedure for producing high efficiency blazed diffraction gratings that takes advantage of the slope selection that results from bombardment with a broad ion beam at a relatively high angle of incidence [23]. In the first stage of their

proposed fabrication method, conventional lithography is used to produce a periodic height modulation on the surface of the sample. The second stage consists of bombarding this pre-patterned surface with a broad ion beam of noble gas ions at a high angle of incidence. HB's simulations strongly suggest that this serves to transform the initial pattern into the periodic sawtooth form characteristic of high quality blazed gratings if the ion beam and target material are selected appropriately. More recently, HB have shown how their fabrication procedure can be extended to produce multilayer blazed gratings that could perform well in the extreme ultraviolet and soft X-ray regimes [24].

In this paper, we will carry out an in-depth study of the terraced topographies produced by ion bombardment of a surface that is nominally flat initially. We begin with the case in which the surface height does not vary in the direction transverse to the projected ion beam direction and the surface is governed by the PB equation of motion. We find that the surface is not completely flat between the undercompressive shocks: instead, small amplitude ripples propagate along the surface in these regions. Our analytical work on these ripples yields their propagation velocity as well as the scaling behavior of their amplitude. These predictions are in good agreement with our numerical integrations of the PB equation. In addition, our simulations establish that the terraced surfaces exhibit interrupted coarsening, i.e., the characteristic width and height of the surface disturbance grow for a time but ultimately asymptote to finite values. Finally, we find that as the coefficient of the cubic nonlinearity γ is reduced, the time needed for a terraced morphology to develop increases and then diverges at a critical value $\gamma_c > 0$. For $0 < \gamma < \gamma_c$, the surface is not terraced and it appears to display spatiotemporal chaos akin to that seen in solutions to the KS equation. Because γ increases with the angle of incidence θ for a range of θ values [21], a transition from an unterraced to a terraced topography could occur in a sequence of experiments in which θ is systematically increased.

We next study an equation of motion that generalizes the PB equation to the case in which the surface height can vary in both the transverse and longitudinal directions. This extended equation of motion produces terraced ripple morphologies that undergo interrupted coarsening, just as the PB equation does. For different ranges of the parameters, it yields other topographies that are remarkably similar to those seen in experiments. For example, for a certain range of the parameters, the extended equation of motion produces pyramidal structures which protrude from the surface and that are elongated in the projected ion beam

direction. Analogous topographies were observed by Carter *et al.* when they bombarded a silicon sample with a 40 keV argon ion beam with a 70° angle of incidence [8]. Teichmann *et al.*, on the other hand, bombarded silicon with xenon ions that had an energy of 1.2 keV and a 75° angle of incidence [18]. The isolated lens-shaped depressions they observed are very similar to structures found in numerical integrations of our extended equation of motion.

This paper is organized as follows. In Sec. II, we develop the equation of motion we will employ to model the bombardment of an elemental material with a noble gas ion beam. The behavior of the surface for the case in which the surface height does not depend on the transverse coordinate y is studied in Sec. III. In Sec. IV, we move on to study the surface in the general case in which its height depends on both the longitudinal coordinate x and the transverse coordinate y. We discuss our results and give our conclusions in Sec. V.

II. EQUATION OF MOTION

Consider an initial surface that is perturbed slightly from a completely flat state. We define the $x-y$ plane so that the unperturbed surface lies in it. Furthermore, we orient the x axis so that the ion beam direction lies in the positive quadrant of the $x-z$ plane. The angle of incidence θ is the angle that the ion beam makes with the z axis. We will confine our attention to the case in which the target is an elemental material and the beam consists of noble gas ions. We will assume that the target material is amorphous or that a surface layer is amorphized by the impacting ions.

Let $h(x,y,t)$ be the height of the surface above the point (x,y) in the $x-y$ plane at time t. The most widely used equation of motion (EOM) for the solid surface is

$$u_t = \alpha u_x + \kappa_1 u_{xx} + \kappa_2 u_{yy} - B\nabla^2\nabla^2 u + \lambda_1 u_x^2 + \lambda_2 u_y^2, \tag{1}$$

where $u = u(x,y,t)$ is the deviation of $h(x,y,t)$ from its unperturbed steady-state value [1, 5, 6]. The subscripts on u indicate partial derivatives, and the coefficients α, κ_1, κ_2, B, λ_1 and λ_2 depend the ion species, energy and angle of incidence and on the choice of target material. Equation (1) will be referred to as the two-dimensional anisotropic Kuramoto-Sivashinsky (AKS) equation since u depends on two spatial coordinates.

The only effect that the term αu_x in Eq. (1) has is to cause surface features to propagate laterally at constant velocity. This term can be eliminated by a Galilean transformation,

and so it will be dropped. We will assume that κ_1 and/or κ_2 is negative, so that a flat initial surface is unstable. In this case, the AKS equation generates ripples with an exponentially growing amplitude at early times. If $\kappa_1 < \kappa_2$, then the ripple's wave vector is parallel to the projection of the ion beam onto the $x - y$ plane. These ripples are therefore called parallel-mode ripples. Conversely, if $\kappa_2 < \kappa_1$, then the ripple's wave vector is perpendicular to the projection of the ion beam onto the $x - y$ plane and the ripples are referred to as perpendicular-mode ripples.

We will assume that $\lambda_1 \lambda_2 > 0$ so that unphysical cancellation modes in which the ripple amplitude grows without limit do not occur [25]. The quadratic nonlinearities in Eq. (1) then eventually control the exponential growth, the ripple amplitude saturates, and the surface exhibits spatiotemporal chaos [6]. At any instant during the chaotic behavior, the surface is statistically invariant under the two transformations $x \to -x$ and $y \to -y$. Additionally, the surface does not coarsen according to this model. These observations are significant because experiments carried out at high angles of incidence produce terraced topographies that are not statistically invariant under the transformation $x \to -x$ and that coarsen [7–20]. Since the AKS equation fails to reproduce these two important effects, it is insufficient to model the dynamics produced in these experiments.

In this paper, we investigate the effects of augmenting Eq. (1) with cubic nonlinear terms proportional to u_x^3 and $u_x u_y^2$. This yields the EOM

$$u_t = \kappa_1 u_{xx} + \kappa_2 u_{yy} - B\nabla^2\nabla^2 u + \lambda_1 u_x^2 + \lambda_2 u_y^2 + \gamma_1 u_x^3 + \gamma_2 u_x u_y^2. \tag{2}$$

The cubic terms in Eq. (2) result from expanding the rate the surface recedes to third order in u_x and u_y; as such, Eq. (2) applies only so long as the surface slope remains small. Equation (2) represents an improvement on the AKS equation (1) since only terms of second order in the slope are retained in the derivation of the latter equation.

When an elemental material is bombarded by a beam of noble gas ions, a number of physical effects can influence the surface dynamics. These effects are sputtering, momentum transfer from the incident ions to atoms near the solid surface [4, 26, 27], surface diffusion, ion-induced surface viscous flow [28] and ion implantation [29, 30]. The cubic terms in the equation of motion (2) do not conserve mass, but momentum transfer, surface diffusion and ion-induced surface viscous flow all do. These effects therefore cannot contribute to the coefficients of the cubic nonlinearities γ_1 and γ_2. This means that sputtering and ion

implantation are the only physical effects that can contribute to γ_1 and γ_2. In Ref. 21, Pearson and Bradley found the contribution of sputtering to γ_1, but they did not consider the contribution of ion implantation.

Note that the terms u_x^3 and $u_x u_y^2$ are unchanged by the transformations $y \to -y$ and $u \to u + \text{const.}$, as they must be. However, they are not invariant under the transformation $x \to -x$, and so Eq. (2) does not in general produce surface morphologies that are statistically invariant under this transformation. As we shall see, Eq. (2) reproduces many features that are observed in experiments in which elemental materials are bombarded with noble gas ions at relatively high angles of incidence, including terraced topographies that are not invariant under the transformation $x \to -x$.

Equation (2) reduces to the PB equation of motion if u does not depend on the transverse coordinate y [21]. It has already been studied by Harrison and Bradley for the case in which the initial surface has a periodic height modulation [24]. In this paper, we will study the complex and intriguing behavior predicted by Eq. (2) when the initial surface is nominally flat.

Equation (2) does not include all terms that are of lower order than u_x^3 and $u_x u_y^2$ and that are invariant under the transformations $y \to -y$ and $u \to u + \text{const}$. In particular, it does not include the terms u_x, u_{xxx}, u_{xyy}, $u_x u_{xx}$ and $u_x u_{yy}$. As we have already mentioned, the term proportional to u_x can be eliminated from the EOM by a Galilean transformation and so it is unnecessary to include it. The influence of a term proportional to u_{xxx} has already been investigated in one dimension (1D): it produces a propagating train of solitons if its coefficient is sufficiently large [31]. Soliton trains are not observed in experiments and we are focused on the formation of terraces, and so we will omit the term u_{xxx} in this work. The effect of a term proportional to $u_x u_{xx}$ has been studied in 1D, and it was found that its inclusion leads to the formation of unphysical singularities in finite time [32]. A detailed investigation of the effects of adding the terms u_{xyy} and $u_x u_{yy}$ to the EOM is left for future study.

Castro *et al.* and Muñoz-García *et al.* have demonstrated that adding a term

$$\sum_{i=1}^{2} \sum_{j=1}^{2} K_{i,j} \frac{\partial^2}{\partial x_i^2} \left(\frac{\partial u}{\partial x_j} \right)^2 \tag{3}$$

to the AKS equation leads to interrupted coarsening [33–35]. They have also shown that this term can arise as a result of mass redistribution near the surface of the solid and have

given explicit expressions for the parameters $K_{i,j}$. This term will be omitted from our EOM because its effects are already well understood and because it is expected to play a less prominent role in the dynamics for high angles of ion incidence. In addition, it does not break the $x \to -x$ symmetry and so cannot produce asymmetric terraced topographies. Finally, as we shall see, Eq. (2) produces interrupted coarsening even though it does not include a term of the form (3).

Eq. (2) does not take shadowing of the incident ions into account. Shadowing occurs if the surface slope u_x exceeds $\cot\theta$ at any point on the surface. If the nonlinearities do not adequately control the amplitude of the pattern and shadowing does occur, the equation of motion (2) no longer applies. In these circumstances, Eq. (2) is valid only for sufficiently early times. The same is true of the widely employed AKS equation (1), however.

It is important to note that shadowing need not occur even at long times. Indeed, in the careful experiments of Engler *et al.* [19], shadowing did not occur, and nevertheless terracing was observed. Our equation of motion (2) applies in just these circumstances. From a mathematical standpoint, shadowing does not occur if the coefficients of the nonlinear terms (λ_1, λ_2, γ_1 and γ_2) are sufficiently large in magnitude.

In order to study Eq. (2), we integrated it numerically using the fourth-order Runge-Kutta exponential time-differencing method of Cox and Matthews, starting with small amplitude white noise as the initial condition [36, 37]. This method uses periodic boundary conditions, which best approximate the physical system which is effectively infinitely extended. The linear terms were computed exactly in Fourier space, while the nonlinear terms were evaluated approximately in real space using finite differencing. The finite differences were central differences accurate to second order in the grid spacing. In the case of our simulations in two dimensions (2D), this means that the partial derivative $\frac{\partial u}{\partial x}(x,y)$ was approximated by

$$\frac{u(x+\Delta x,y)-u(x-\Delta x,y)}{2\left(\Delta x\right)^2}, \tag{4}$$

where Δx is the grid spacing. The temporal step used was $\Delta t = 0.1$ in the 1D simulations, while Δt was 0.0025 in the 2D simulations.

III. TERRACING IN ONE DIMENSION

In this section, we report results and develop predictions for the case in which the surface does not vary in the transverse direction (i.e., u_y vanishes for all x and y). This special case will be referred to as the "one-dimensional case." When u_y is set to zero in Eq. (2) and resulting equation is suitably rescaled, we obtain the PB equation of motion

$$u_t = -u_{xx} - u_{xxxx} - \frac{1}{2}u_x^2 + \frac{1}{6}\gamma u_x^3, \tag{5}$$

where the dimensionless prefactor of the cubic nonlinearity

$$\gamma = \frac{3|\gamma_1 \kappa_1^{3/2}|}{2\lambda_1^2 B^{1/2}} \tag{6}$$

is real and nonnegative. In our numerical work, we will study solutions to Eq. (5) on the spatial interval $0 \leq x \leq L$. The number of spatial grid points will be denoted by N.

A. Small Scale Ripples on Terraces

For sufficiently large values of γ and of the time t, the solutions to Eq. (5) have large regions in which the surface slope is nearly equal to one of the selected values Φ_+ and Φ_-, which are given by

$$\Phi_\pm = \frac{1}{\gamma} \pm \sqrt{\frac{6|s_{\rm tr}|}{\gamma}}, \tag{7}$$

where

$$s_{\rm tr} \simeq -2.3879 \tag{8}$$

is a constant [21]. These regions of nearly constant slope are separated by undercompressive shocks that propagate laterally with the velocity

$$s = s_{\rm tr} + \frac{1}{\gamma}. \tag{9}$$

Hereafter we shall refer to a state in which undercompressive shocks have formed and are connected by regions of approximately constant slope as a "well formed terraced state."

While at long times the large scale behavior is characterized by terrace formation, closer inspection reveals that there exist ripple-like disturbances on the regions of approximately constant slope. Figure 1 shows a typical surface obtained from a low amplitude spatial white

noise initial condition as well as its second spatial derivative as a function of position. By looking at u_{xx}, one can more easily see the deviations from a constant slope. The amplitude and lateral propagation velocity of the small scale ripples may be determined by a close examination of Eq. (5).

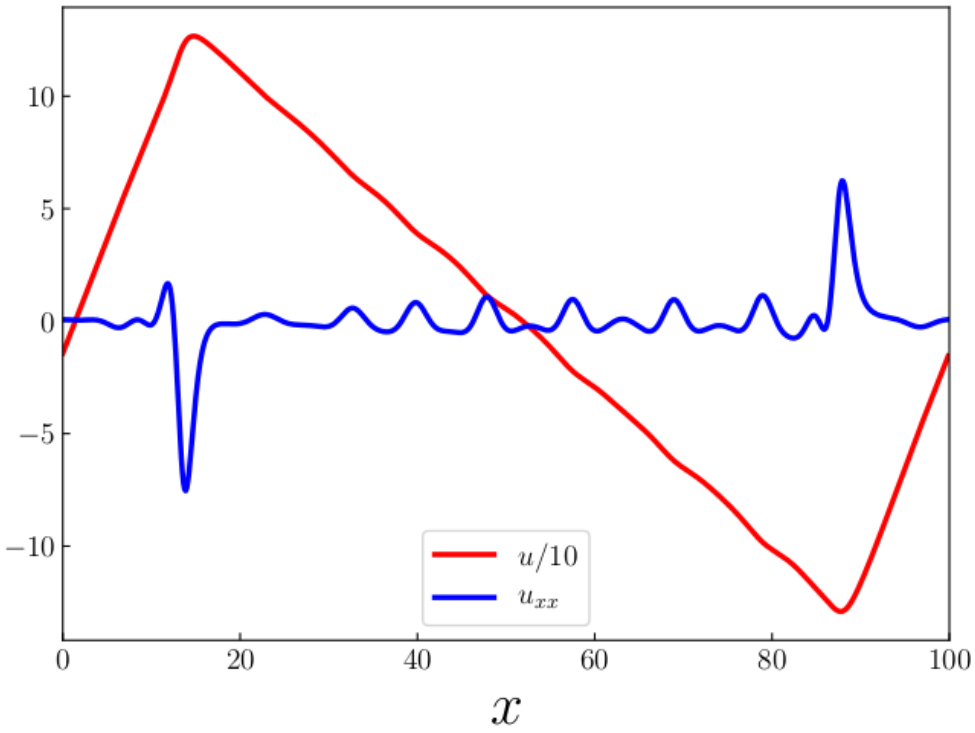

FIG. 1: (Color online) A plot of u for a simulated surface (the red curve) and its second spatial derivative u_{xx} (the blue curve) that shows the formation of small scale ripples on a terraced surface. Note that u has been scaled down for visual clarity. For this simulation, $\gamma = 0.3$ and the elasped time was 10^3. The sample length L was 100 and the number of spatial grid points N was 801.

Consider a surface which has

$$u(x,t) = \Phi_{\pm} x + v(x,t). \tag{10}$$

If v were zero, the surface would have a constant slope equal to one of the two selected slopes Φ_+ and Φ_-. The term $v = v(x,t)$ is the deviation from this state. Although our simulations reveal that v is a small correction in a region of nearly constant slope, we will actually develop predictions which are valid to all orders in v. From Eqs. (5) and (10) we

obtain the EOM

$$v_t = \hat{L}v - \frac{1}{2}(v_x + \Phi_\pm)^2 + \frac{\gamma}{6}(v_x + \Phi_\pm)^3, \tag{11}$$

where

$$\hat{L} \equiv -\partial_x^2 - \partial_x^4. \tag{12}$$

Collecting terms, Eq. (11) becomes

$$v_t = \hat{L}v + c_0 + c_1 v_x + c_2 v_x^2 + \frac{\gamma}{6} v_x^3, \tag{13}$$

where

$$c_0 = -\frac{1}{2}\Phi_\pm^2 + \frac{\gamma}{6}\Phi_\pm^3 = -\frac{1}{3\gamma^2} \pm \frac{\sqrt{6|s_{\rm tr}|}}{2\gamma^{\frac{3}{2}}}\left(2\gamma|s_{\rm tr}| - 1\right), \tag{14}$$

$$c_1 = -\Phi_\pm + \frac{\gamma}{2}\Phi_\pm^2 = -\frac{1}{2\gamma} + 3|s_{\rm tr}|, \tag{15}$$

and

$$c_2 = -\frac{1}{2} + \frac{\gamma}{2}\Phi_\pm = \pm\frac{1}{2}\sqrt{6|s_{\rm tr}|\gamma}. \tag{16}$$

The first conclusion that may be drawn from Eqs. (13) - (16) is that the small scale ripples have a nonzero lateral propagation velocity equal to $-c_1$. A spacetime plot of local maxima of u_{xx} is given in Fig. 2; this shows the propagation of the small scale ripples well. A line with slope equal $-c_1$ is included in the figure; it is close to being parallel to the lines traced out by the local maxima of u_{xx}, and so the predicted lateral propagation velocity for the small scale ripples is in good accord with the results of our simulation. This velocity is the same for the small scale ripples which form on both selected slopes. This too is in agreement with our simulation. Finally, the line with the steeper slope in Fig. 2 has a slope equal to the predicted shock propagation velocity given by Eq. (9). This is also in satisfactory agreement with our simulation.

Turning now to the question of the amplitude of the ripples, we transform Eq. (13) to a moving frame of reference in order to eliminate c_0 and c_1. Explicitly, we set

$$\tilde{v} = v + c_0 t \tag{17}$$

and

$$\tilde{x} = x + c_1 t. \tag{18}$$

The resulting EOM, upon suppression of the tildes, is given by

$$v_t = \hat{L}v \pm \frac{1}{2}(6|s_{\rm tr}|\gamma)^{\frac{1}{2}} v_x^2 + \frac{\gamma}{6} v_x^3. \tag{19}$$

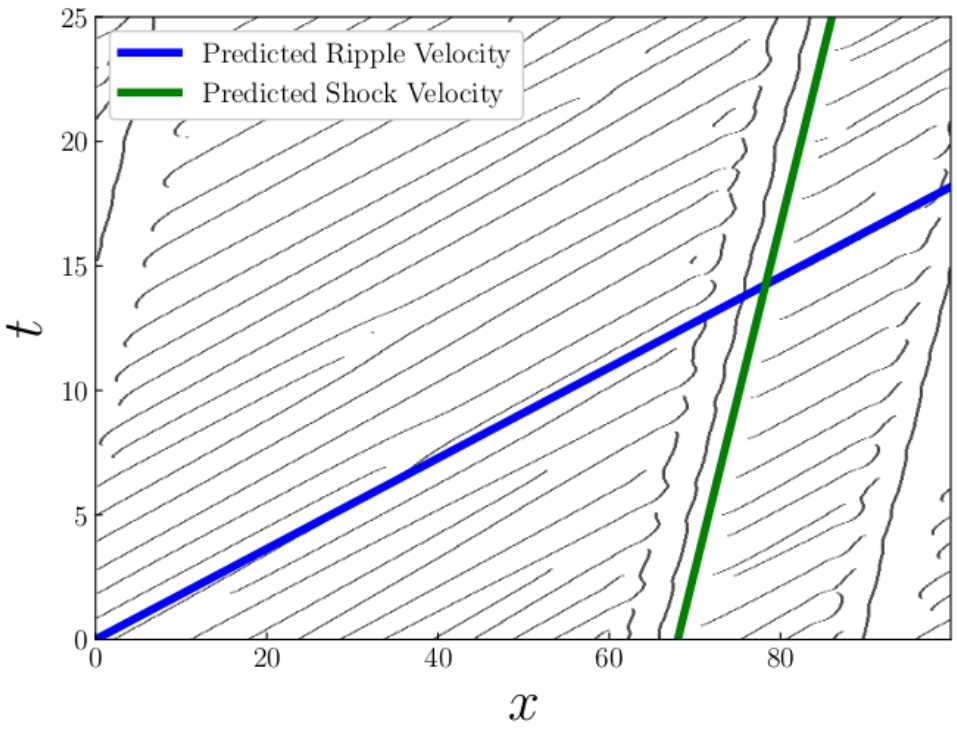

FIG. 2: (Color online) A spacetime plot of the local maxima of u_{xx}. The blue and green overlayed lines have slopes equal to the predicted propagation velocities of the small scale ripples and shocks, respectively. The simulation parameters were $\gamma = 0.3$, $L = 100$ and $N = 801$. The initial condition was low amplitude spatial white noise.

Because the coefficient of v_x^2 in Eq. (19) has equal magnitude but opposite sign on surfaces with the two selected slopes, we expect that ripples that form on terraces with average slope Φ_+ will be inverted (i.e., $v \to -v$) relative to ripples that form on terraces with average slope Φ_-. These ripples nevertheless possess exactly the same propagation velocity. The qualitative relationship between the shape of ripples on the positive and negative selected slopes is evident in our simulation results (not shown here).

We bring Eq. (19) to a parameter free form via the substitution

$$v = \mp \frac{w}{\sqrt{6|s_{\rm tr}|\gamma}}, \tag{20}$$

which yields

$$w_t = \hat{L}w - \frac{1}{2}w_x^2 + \frac{1}{36|s_{\rm tr}|}w_x^3. \tag{21}$$

A couple of comments about Eq. (21) are in order: Firstly, it is equivalent to Eq. (5) for the case in which $\gamma = (6|s_{\rm tr}|)^{-1}$. Equation (21) does not form a terraced surface if the

initial condition is low amplitude spatial white noise because one of the two selected slopes predicted for this value of γ is equal to zero. Secondly, Eq. (21) does not depend on γ. We can therefore predict how the characteristic amplitude of the small scale ripples on terraces scales with γ. Referring to Eq. (20), we see that the amplitude of the small scale ripples on the terraces should scale as $1/\sqrt{\gamma}$.

This result is interesting in its own right, since it provides insight into how the terraces persist indefinitely despite being linearly unstable. The terraces develop small scale ripples whose amplitude eventually saturates to a value that is proportional to $1/\sqrt{\gamma}$. Higher values of γ therefore lead to surfaces which are better approximated by regions of exactly constant slope connected by undercompressive shocks.

This analysis also highlights an important subtlety of describing solutions to Eq. (5). The relative positions of the shocks do not change appreciably once the surface has developed into a well formed terraced state. However, it is not accurate to describe such a state as stable, because as we have just demonstrated that the regions of approximately constant slope are in fact linearly unstable. For this reason, we may only say that solutions to Eq. (5) may be *approximated* by a steady-state solution, with the error in this approximation stemming from the small scale ripples on the terraced faces.

One means of characterizing the approximate steady states attained by solutions to Eq. (5) will be referred to as the "correlation metric" $C(t)$. Let $\langle u(t) \rangle$ denote the spatial average of $u(x,t)$ and set $w(x,t) = u(x,t) - \langle u(t) \rangle$. The correlation metric $C(t)$ is defined as follows:

1. Chose a reference surface $w_{\text{ref}}(x) \equiv w(x, t_{\text{ref}})$ at a sufficiently late time t_{ref} that a well formed terraced state has developed.

2. Consider the surface at some time t, given by $w(x,t)$. Both w and w_{ref} are subject to periodic boundary conditions [i.e., $w(x,t) = w(x+L,t)$, where L is the sample length].

3. Consider the function $\tilde{C}(t,i) \equiv \Sigma_{j=1}^{N} |w(x+j\Delta x, t) - w_{\text{ref}}(x+j\Delta x + i\Delta x)|/N$, where N is the number of gridpoints, $\Delta x \equiv L/N$ is the grid spacing, and i and j are integers that range from 1 to N.

4. Define the correlation metric $C(t)$ to be the minimum value of $\tilde{C}(t,i)$, where i ranges from 1 to N.

If the surface attained a steady-state form that simply translated laterally and downward, $C(t)$ would be equal to zero for sufficiently long times. This does not occur because of the small scale ripples on the terraces. However, $C(t)$ is relatively small when the large scale terrace features in the surface at time t have nearly the same form as those in the reference state.

The small scale ripples that form on the terraces seem to exhibit spatiotemporal chaos similar to the solutions of the KS equation. This is reflected in the apparently chaotic variations in the value of $C(t)$. A plot that shows the time dependence of $C(t)$ for a well formed terraced state is shown in Fig. 3.

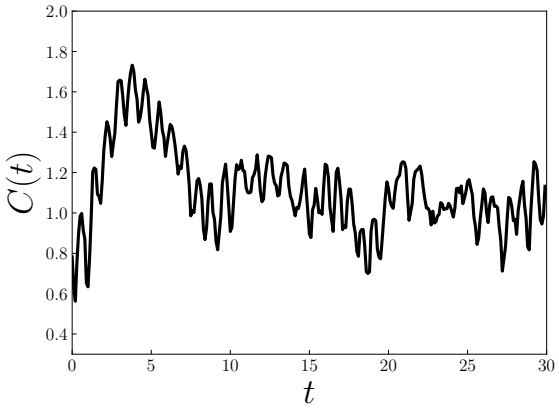

FIG. 3: $C(t)$ versus time for a well formed terraced state. The simulation parameters were $\gamma = 1$, $L = 100$ and $N = 801$. The reference time $t_{\rm ref}$ was 120.

We have argued that the amplitude of the small scale ripples on the terraces should scale as $1/\sqrt{\gamma}$. In a well formed terraced state, the only contribution to $C(t)$ is expected to come from these ripples. We therefore expect that the temporal average value of $C(t)$ for a well formed terraced state should also scale as $1/\sqrt{\gamma}$. From Fig. 4 we see that this is in fact the case.

B. Interrupted coarsening

Having analyzed the small scale ripples that form on the terraces, we now concentrate on the large scale terraces themselves. One of the most interesting features of solutions to Eq. (5) is that their characteristic amplitude and horizontal length scale grow for a time, and then asymptote to approximate steady-state values. In what follows, we will

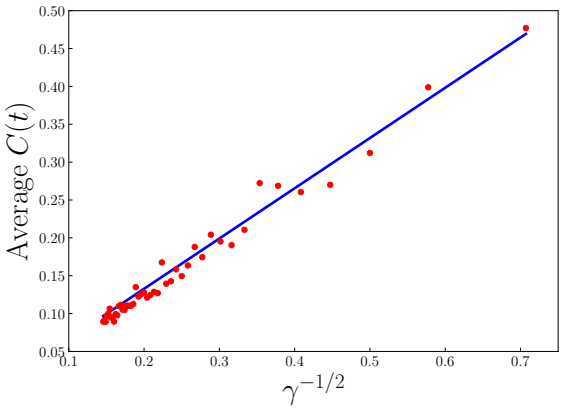

FIG. 4: (Color online) The temporal average value of $C(t)$ from $t = 125$ to $t = 250$ (vertical axis) for well formed terrace states over a range of γ values (horizontal axis). The reference time is $t_{\text{ref}} = 250$. The blue line shows the fit to the form $b_1\gamma^{-1/2}$, with $b_1 = 0.6637$, whereas the red points are individual simulation results.

characterize this approximate steady state by the number of local extrema on the surface. Our numerical simulations indicate that once solutions to Eq. (5) have evolved into a state in which every extremum is an undercompressive shock, the number of extrema does not change. Additionally, the density of extrema seems to be independent of the sample size provided that the sample size is much larger than the linearly selected wavelength. Figure 5 shows the average density of local maxima for solutions to Eq. (5) for a range of domain lengths with low amplitude white noise initial conditions.

One interesting feature of the interrupted coarsening is how rapidly the transition between exponential growth and the approximate steady state occurs. Figure 6 (a) shows the surface width σ as a function of time averaged over 500 simulations. Initially, the time evolution is dominated by the linear terms in the EOM, giving rise to exponential growth in σ. Over a short period of time, the amplitude grows enough that the nonlinear terms begin to dominate, and the growth of the surface width ceases.

Figure 6 (b) shows evidence of interrupted coarsening in the lateral direction. A characteristic wave number k_{max} was obtained by computing the average wave number of the largest amplitude Fourier mode. At early times, the surface develops a periodic structure whose characteristic wave number is selected by the linear terms in Eq. (5). However, once the surface amplitude grows large enough that the nonlinear terms become important, the characteristic length increases (i.e., k_{max} decreases). This coarsening does not persist indef-

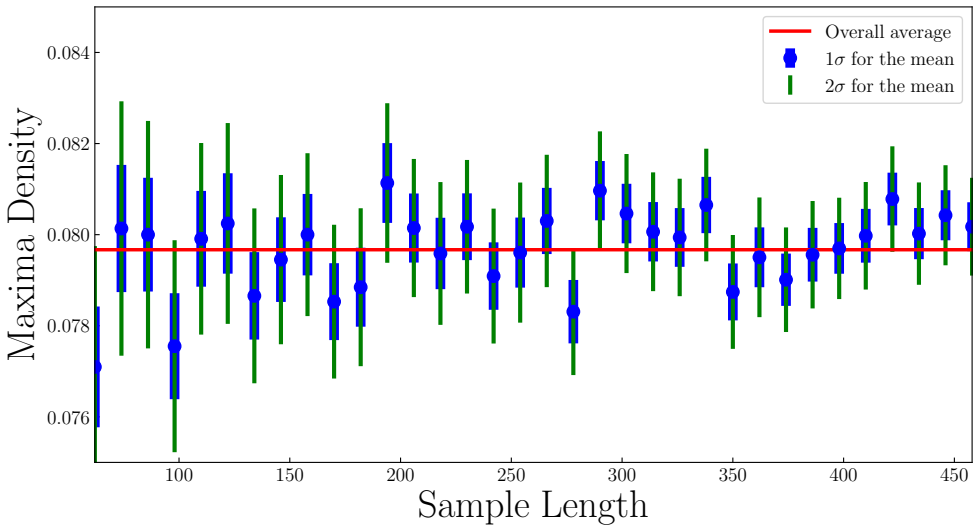

FIG. 5: (Color online) A plot of the density of local maxima as a function of the sample length for $\gamma = 1$. Notice the minimal variation over the range shown. This indicates that the density of maxima is likely independent of the sample length L for sufficiently large L. The error bars show the standard deviation in the density of local maxima at $t = 500$ in 200 simulations.

initely, and the surface eventually evolves into a state with a constant characteristic length.

Once an approximate steady state has been achieved, the degree to which the large scale structure of solutions to Eq. (5) remains unchanged as they translate downward and laterally is striking. To see this, we transform to a co-moving frame of reference with a lateral velocity s and downward velocity μ given by Eqs. (43) and (50) of Ref. [21], respectively. Figure 7 shows plots of the surface in the comoving frame at thousands of different times. It is clear that once the surface adopts its asymptotic shape, there is very little subsequent variation within a single simulation. If we compare simulations with different white noise initial conditions, we find an appreciable variation in the asymptotic surface shape, however.

C. Time to Form an Approximate Steady State

One observed feature of solutions to Eq. (5) is that the terracing behavior is strongly dependent upon the value of γ. Previous work [21] showed that the value of this coefficient determines the selected slopes and propagation velocity of the terraced state that forms. However, if the equations developed in that work are taken to hold in the limit $\gamma \to 0$, they

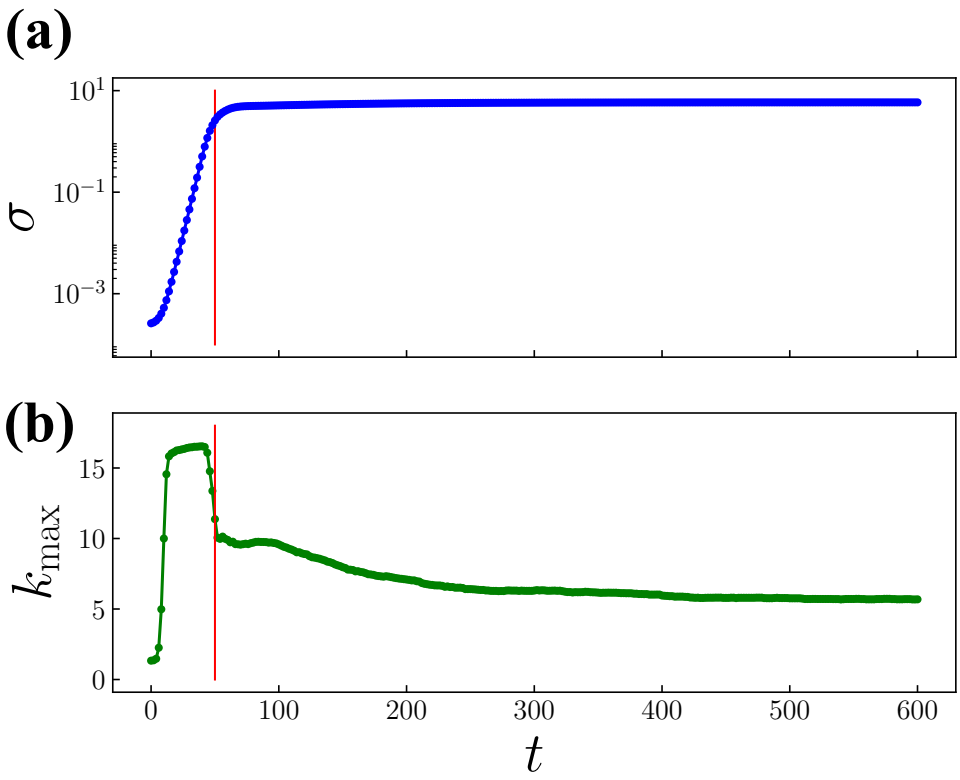

FIG. 6: (Color online) A semilog plot of the standard deviation of the surface height σ [panel (a)] and a plot of the average wave number of the largest amplitude Fourier mode $k_{\max}$ [panel (b)] for solutions to Eq. (5). The points shown each represent an average over 500 simulations. The simulation parameters were $\gamma = 1$, $L = 150$ and $N = 251$. The vertical red line is shown as a guide to the eye; it appears at a time when the rapid crossover from the linear to the nonlinear regime is taking place. The value of k with the highest linear growth rate was $k = L/(\sqrt{8}\pi) \simeq 16.88$.

give impossible predictions. In particular, for $\gamma < (6|s_{\rm tr}|)^{-1} \simeq 0.07$, the two selected slopes have the same sign, and as γ decreases, the predicted lateral propagation and downward drift velocities grow without limit.

Obviously, as γ decreases in magnitude, the importance of the γu_x^3 term decreases, and it will not lead to lateral and downward propagation at an infinite rate. The unphysical predictions of the analysis in Ref. [21] in the limit $\gamma \to 0$ do not arise from a flaw in the analysis, but rather are a consequence of the assumption that a terraced state forms. For small values of γ, the surface behaves similarly to the KS equation, and does not evolve into a well formed terraced state. In this section, we explore the necessary condition on γ for a

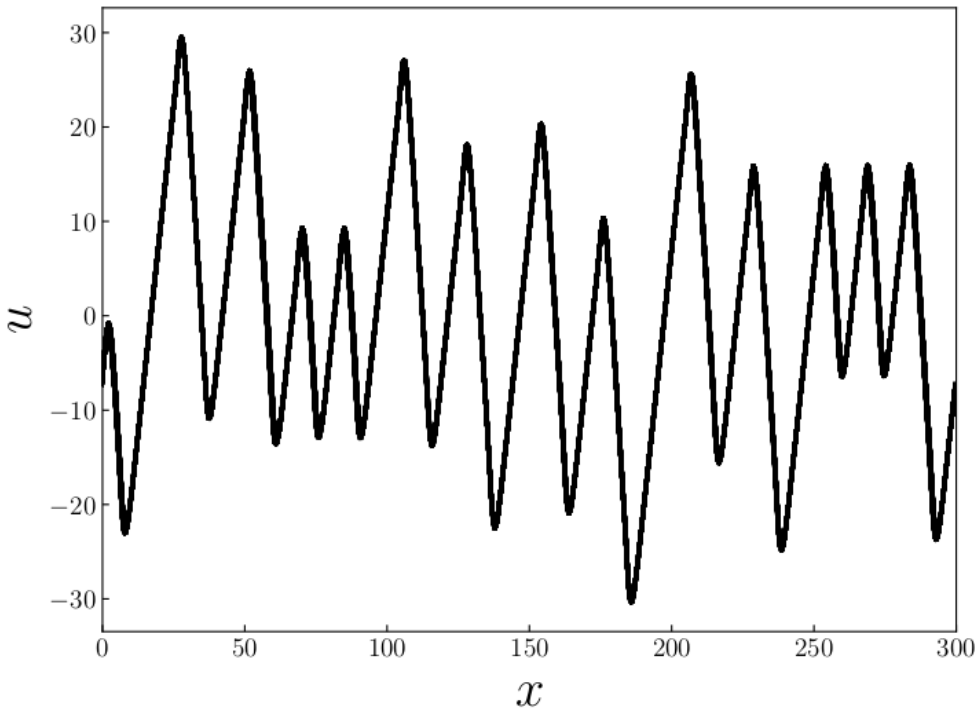

FIG. 7: 2000 snapshots of a typical surface overlayed in the co-moving frame of reference with $\gamma = 1$. The snapshots were taken one time unit apart from $t = 1000$ to $t = 3000$. There is very little variation in the large scale form of the surface once a terraced state has been achieved. The values of L and N were 300 and 541, respectively.

terraced state to develop from a low amplitude spatial white noise initial condition and for the equations developed in Ref. [21] to apply.

In order to analyze the transition from terraced states to KS-like behavior as γ is reduced, it is necessary to develop a metric that allows us to distinguish these two kinds of states. One of the primary distinctions between the two is in the time dependence of the number of local maxima. Local maxima and minima in a terraced state are present only at the shocks since the amplitude of the small scale ripples is too small relative to the selected slopes Φ_+ and Φ_- for there to be extrema at their crests and troughs. Once the approximate steady state is attained, the number of local maxima does not change. In a KS-like state, by contrast, local maxima and minima are constantly appearing and disappearing. We identify terraced states by looking at the number of local maxima versus time. If the number of maxima is unchanged over a threshold length of time, we declare that a terraced state has formed, and record the last time at which the number of maxima changed. By setting this threshold

rather high ($t = 10^3$ for the results reported here), we can reliably differentiate between terraced and non-terraced states.

Figure 8 shows the results of over 12,000 simulations for a range of values of γ. Even on a semilog plot, the singular behavior is striking. The red curve shows a fit to the functional form

$$T_{\rm tf} = \exp\left[\beta(\gamma - \gamma_c)^\alpha + \Delta\right], \tag{22}$$

where $T_{\rm tf}$ is the time taken to form a terraced state starting from a low amplitude spatial white noise initial condition and α, β, γ_c, and Δ are fitting parameters. The fitted values in Fig. 8 are $\alpha = -0.425$, $\beta = 0.527$, $\Delta = 3.900$ and $\gamma_c = 0.277$. Based on these simulations, we estimate that the critical value of γ is $\gamma_c = 0.277$. Interestingly, this is very close or equal to the value of γ where the negative selected slope Φ_- takes on its minimum value [21].

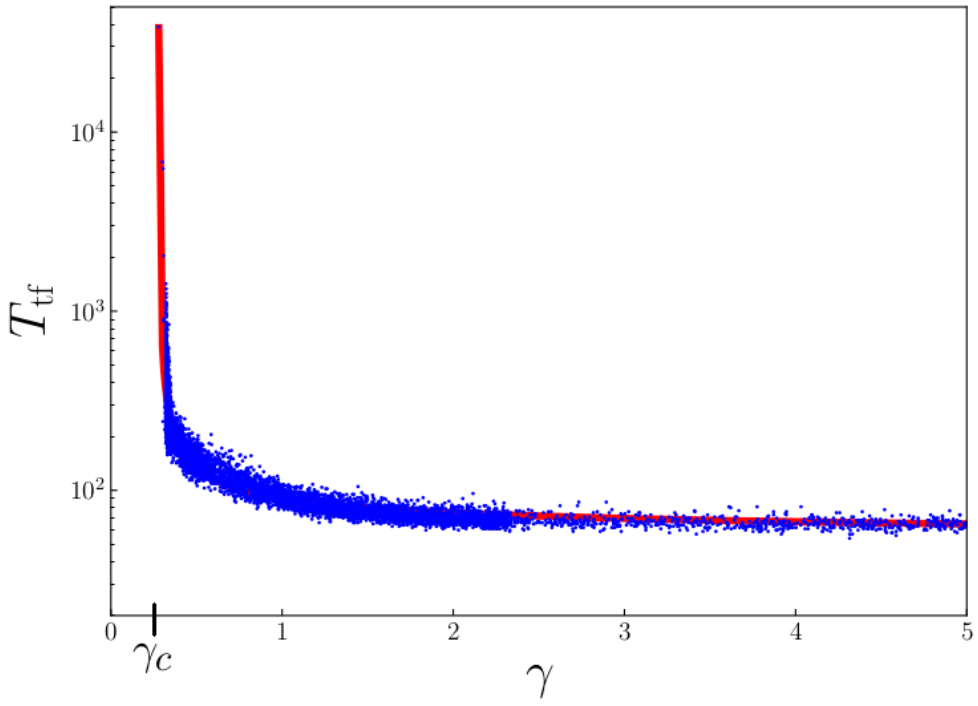

FIG. 8: (Color online) The time taken for individual surfaces to reach a well formed terraced state (blue dots) and the fit to the form given by Eq. (22) (red curve). The optimal fit was obtained for $\alpha = -0.425$, $\beta = 0.527$, $\Delta = 3.900$ and $\gamma_c = 0.277$.

IV. TERRACING IN TWO DIMENSIONS

So far, we have studied the solutions to Eq. (2) for the special case in which u is independent of the transverse coordinate y, i.e., the 1D case. We will now explore the behavior predicted by Eq. (2) when u depends on x, y and t. We will refer to this as the 2D case.

In Ref. [21], Pearson and Bradley demonstrated that including the cubic nonlinearity u_x^3 in the EOM can lead to terrace formation in 1D, but the question of whether this also holds true in 2D was not addressed. In this section, we present simulation results in 2D which display topographies that are terraced analogs of parallel-mode ripples. In addition, we find that inclusion of the cubic nonlinearities u_x^3 and $u_x u_y^2$ in the EOM can yield surface morphologies that resemble those observed in various experiments. Among these are elongated pyramidal structures [8, 20] and lenticular depressions [18]. We also compare the predictions from the 1D theory with our simulations in 2D when there is smoothing in the transverse direction and find that key predictions from 1D carry over to 2D.

A. Parallel-Mode Terraces

The most significant effect of including the cubic nonlinearity u_x^3 in the EOM (2) is that it can lead to the formation of a terraced topography. The results of a simulation in 2D are shown in Fig. 9. The topographies that develop are quite similar to those found in an experiment in which a silicon sample was irradiated with a 60 keV Ar^+ ion beam with a 60° angle of incidence (see Fig. 1 of Ref. [10]). In both the experiments and the simulations, terraces develop that resemble parallel-mode ripples, except that the regions between the crests and troughs have nearly constant slope. We call these structures *parallel-mode terraces*, in analogy with parallel-mode ripples. Figure 10 shows the mean curvature, which we shall denote by H, for the surface in Figure 9 (b); the distinctive nearly vertical dark and light lines are undercompressive shocks that are associated with terrace formation. In between these shocks is a complicated cellular structure of small scale ripples. Small scale ripples are ubiquitous in simulations with $\kappa_1 < 0$ and $\kappa_2 < 0$ once terraces have formed.

From Fig. 11 we see that the gradient distribution for Fig. 9 (b) (i.e., a 2D histogram of u_x and u_y values) has two preferred values for u_x: this confirms that the surface is indeed terraced. The spread in u_y occurs because of the transverse instability; if κ_2 were positive

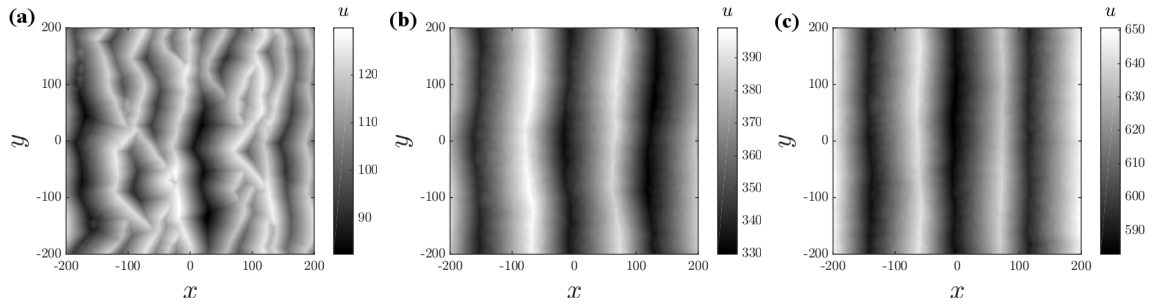

FIG. 9: The surface height obtained from a simulation of Eq. (2) at times (a) $t = 1000$, (b) $t = 3000$ and (c) $t = 5000$. By the end of the simulation, parallel-mode terraces have developed, with slight bends in the terrace edges due to the presence of a transverse instability. The parameter values used were $\kappa_1 = -0.5$, $\kappa_2 = -0.1$, $\lambda_1 = 0.5$, $\lambda_2 = 0.5$, $B = 1$, $\gamma_1 = 1$ and $\gamma_2 = 0$.

instead of negative, the gradient distribution would be strongly peaked in the transverse direction at long times.

B. Steady-state solutions

In the 1D theory, the terraced solutions are traveling waves which propagate and descend at a constant rate. We assume the same to be true of the terraced solutions to Eq. (2). Thus, we seek solutions to Eq. (2) of the form $u(x, y, t) = f(x - st, y) - \mu t$, where f is a function that gives the shape of the traveling wave, s is the lateral propagation velocity and μ is the downward drift speed. This yields the following time-independent partial differential equation:

$$\kappa_1 f_{xx} + \kappa_2 f_{yy} - B\nabla^2\nabla^2 f + \lambda_1 f_x^2 + \lambda_2 f_y^2 + \gamma_1 f_x^3 + \gamma_2 f_x f_y^2 + s f_x + \mu = 0. \tag{23}$$

Since a terraced surface is dominated by regions of constant slope, we seek solutions in which the surface is flat, i.e., in which $u_{xx} = u_{xy} = u_{yy}$. Thus, we expect that the terraced surfaces' gradient distributions are most heavily weighted at the values of (f_x, f_y) satisfying the algebraic equation

$$\lambda_1 f_x^2 + \lambda_2 f_y^2 + \gamma_1 f_x^3 + \gamma_2 f_x f_y^2 + s f_x + \mu = 0. \tag{24}$$

The set of points (f_x, f_y) satisfying Eq. (24) is the union of up to three nonintersecting curves. The gradient distributions are concentrated close to two subsets of these curves, as

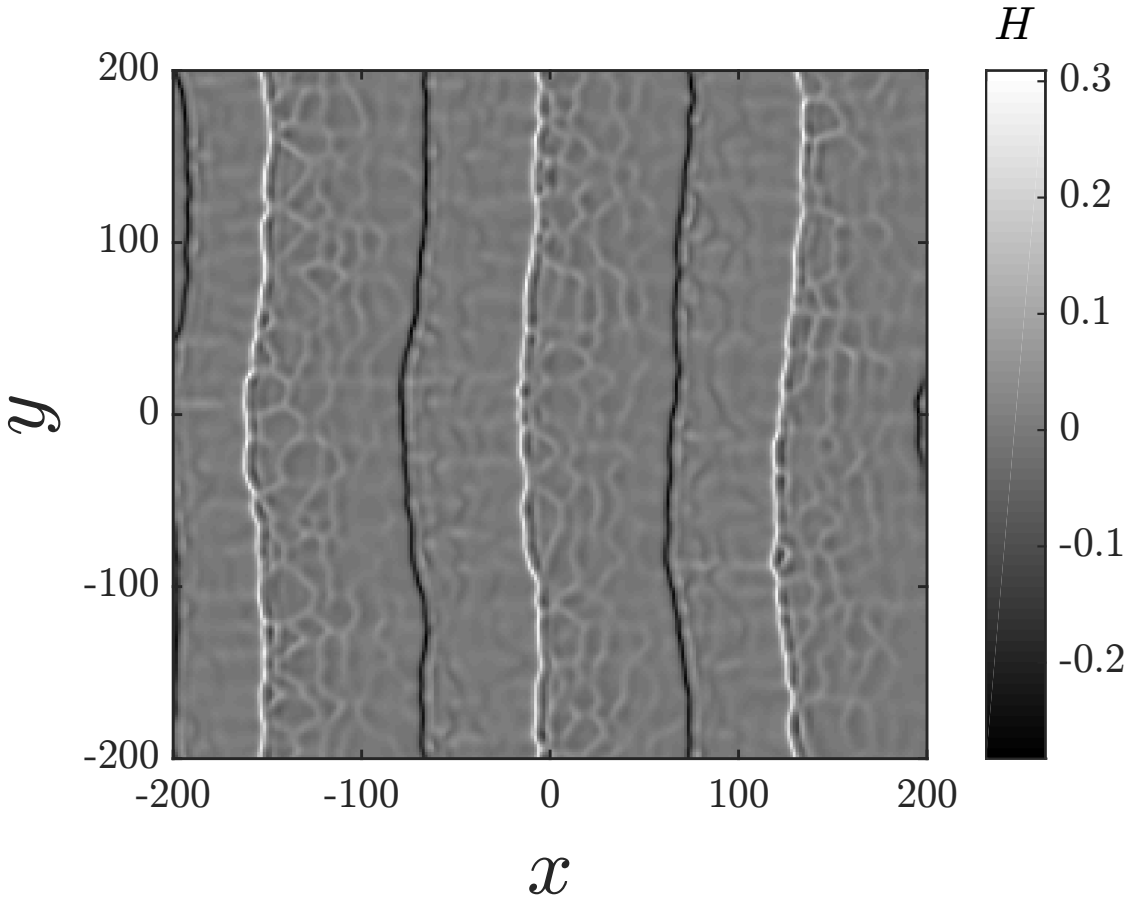

FIG. 10: The mean curvature of a surface obtained from a simulation of Eq. (2) at time $t = 3000$. The figure shown is the mean curvature of the surface seen in Figure 9 (b).

shown in Fig. 12 for three different sets of parameter values. This is in direct analogy with the 1D case in which there are only two selected slopes even though there are three zeros for the cubic equation which yields the selected slopes [21].

Simulations of Eq. (2) with different values of κ_1 and κ_2 (and with all other coefficients held fixed) produce surfaces with gradient distributions that are more heavily weighted on different subsets of the curves satisfying Eq. (24). This is illustrated in Figs. 12 (a) and (b), which are gradient distributions obtained from two surfaces produced by simulations with different values of κ_2 but the same parameter values $\kappa_1 = \lambda_1 = \lambda_2 = -0.5$, $B = 1$, $\gamma_1 = 1$ and $\gamma_2 = 0$. Equation (24) also works well if γ_2 is nonzero, as can be seen in Fig. 12 (c), which was obtained from a simulation with coefficient values $\kappa_1 = 0$, $\kappa_2 = -0.5$, $\lambda_1 = \lambda_2 = -0.5$, $B = 1$, $\gamma_1 = 1$ and $\gamma_2 = -1$. The values of s and μ used to produce the red curves in these figures were determined directly from the simulations. The method we employed to

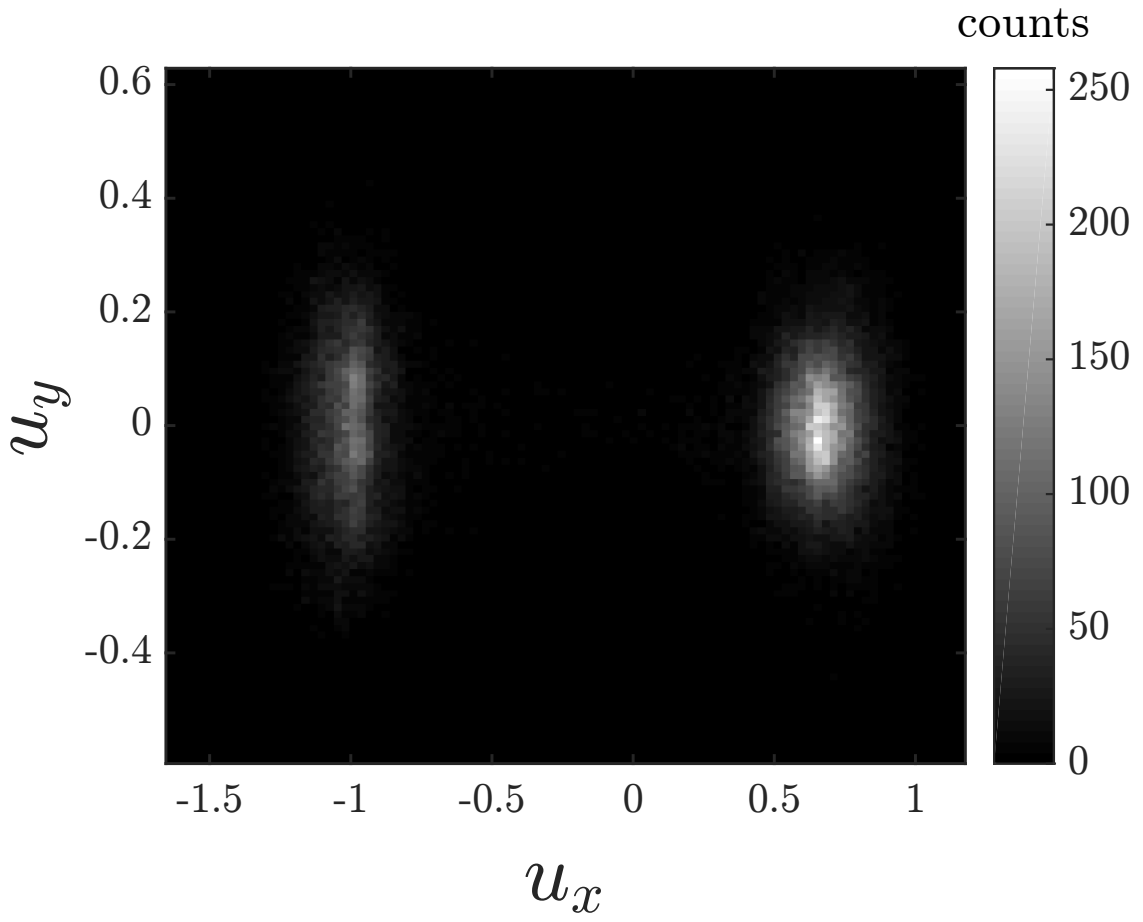

FIG. 11: The gradient distribution of the surface obtained from a simulation of Eq. (2) at time $t = 3000$. The figure shown was obtained from the surface seen in Fig. 9 (b).

compute s is the same as that introduced in Ref. [21]; essentially, we calculated the lateral shift that minimizes the difference between the surface at two different times. We calculated an average s by comparing the surface at each of the final 10 time steps with the surface at its previous time step. The values of μ were determined by the slope of a linear fit of the average value of u versus time during the last 10 time steps.

C. Comparison with the predictions of the one-dimensional theory

We now investigate how well the predictions made in Ref. [21] for the 1D case apply to simulations in 2D, with a focus on the case in which there is smoothing in the transverse direction. Figure 13 shows a line scan along the x axis of a surface obtained by integrating Eq. (2) with the parameter values $\kappa_1 = -0.5$, $\kappa_2 = 1$, $\lambda_1 = -5$, $\lambda_2 = -5$, $B = 1$, $\gamma_1 = 100$

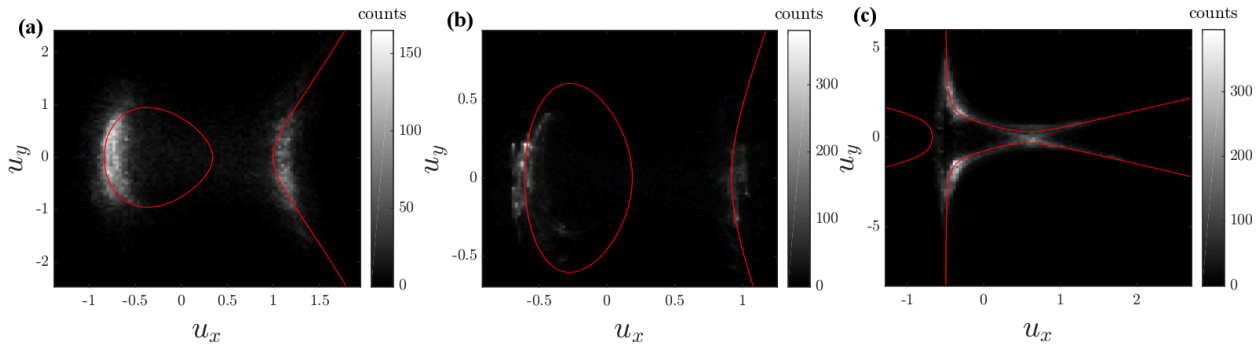

FIG. 12: (Color online) The gradient distributions of three surfaces obtained from a simulation of Eq. (2) integrated up to time $t = 750$ with the solutions to Eq. (24) plotted as red curves. The parameter values used in the simulations were (a) $\kappa_1 = -0.5$, $\kappa_2 = -0.5$, $\lambda_1 = -0.5$, $\lambda_2 = -0.5$, $B = 1$, $\gamma_1 = 1$ and $\gamma_2 = 0$; (b) $\kappa_1 = -0.5$, $\kappa_2 = 0.5$, $\lambda_1 = -0.5$, $\lambda_2 = -0.5$, $B = 1$, $\gamma_1 = 1$ and $\gamma_2 = 0$; (c) $\kappa_1 = -0.5$, $\kappa_2 = 0.5$, $\lambda_1 = -0.5$, $\lambda_2 = -0.5$, $B = 1$, $\gamma_1 = 1$ and $\gamma_2 = -1$.

and $\gamma_2 = 0$. From this figure, it is evident that terraces have formed. Moreover, the line scan is quite similar to surfaces obtained in simulations in 1D [21].

In Ref. [21], Pearson and Bradley derived formulas for the propagation velocity, downward drift speed and selected slopes of the terraces that form on a surface governed by Eq. (5), i.e., a surface which has no transverse variations in height. The selected slopes $\Phi_\pm$ and the propagation velocity s they obtained are given by Eqs. (7) and (9) of this paper. The downward drift speed μ is

$$\mu = -\frac{1}{6\gamma^2} - \frac{s_{\rm tr}}{\gamma}; \tag{25}$$

this is Eq. (50) of Ref. [21].

In Figure 14, we compare $\Phi_\pm$, s and μ as given by Eqs. (7), (9) and (25) with the values obtained from numerical integrations of Eq. (2) as $\gamma \equiv 6\gamma_1$ is varied while the other coefficients are held fixed at the values $\kappa_1 = -1$, $\kappa_2 = 20$, $B = 0$, $\lambda_1 = -0.5$, $\lambda_2 = -0.5$ and $\gamma_2 = 0$. (Note the large positive value of κ_2 we selected.) We used a smaller domain for these simulations so that an approximate steady state would be reached at an earlier time than it was in the figures previously shown. The methods of determining the values of s and μ from the simulations were the same as we discussed earlier in this section. The error bars for s are obtained from the standard deviation of the 10 values averaged to give s. The error bars on μ were calculated from the R-squared value of the linear fit using $\mu_{\rm err} = (1 - R^2)\mu_{\rm value}$.

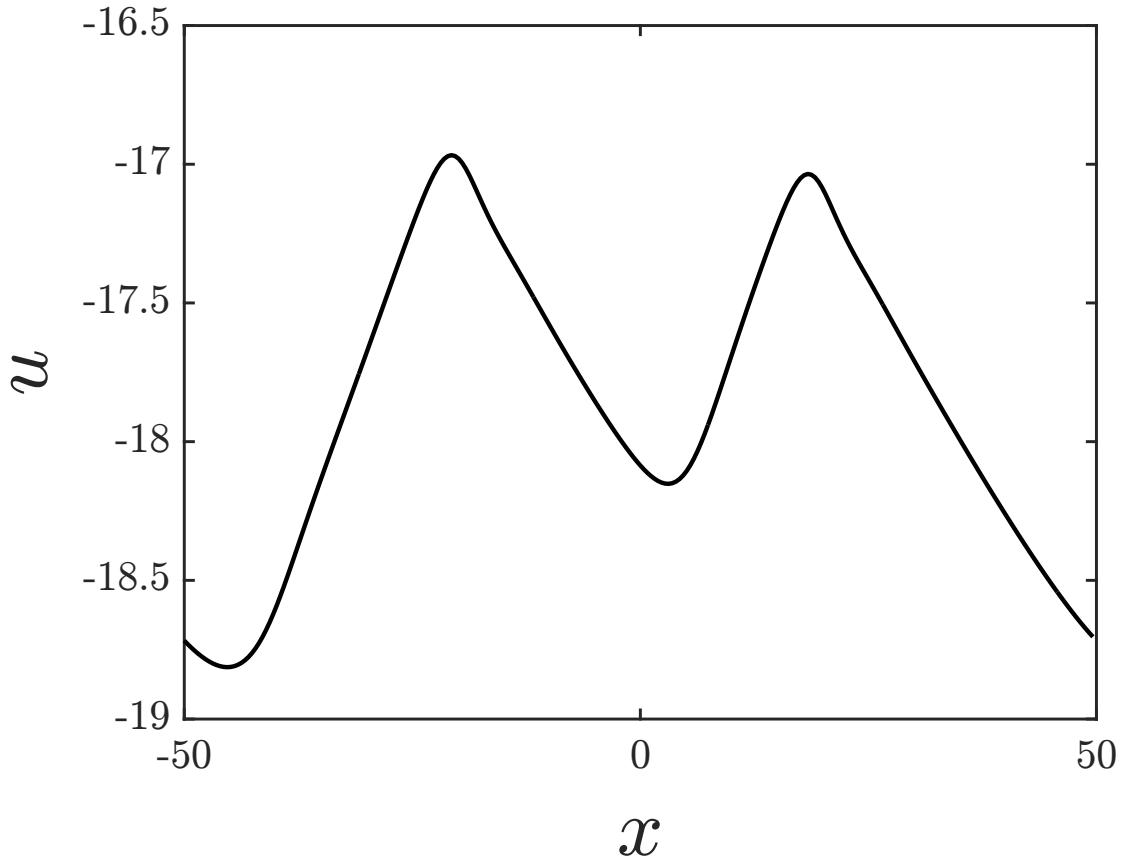

FIG. 13: A line scan along the x axis slice of a surface with transverse smoothing at time $t = 2000$. Note that the vertical scale has been enlarged by a factor of 40 to make the pattern easily discernable; the magnitude of the surface slope nowhere exceeds 0.1. The parameter values used were $\kappa_1 = -0.5$, $\kappa_2 = 1$, $\lambda_1 = -5$, $\lambda_2 = -5$, $B = 1$, $\gamma_1 = 100$ and $\gamma_2 = 0$.

We used the same method as in Ref. [21] to calculate $\Phi_\pm$ from the simulations. The results from the simulations in 2D with strong smoothing in the transverse direction are in excellent agreement with predictions of the 1D theory given by Eqs. (7), (9) and (25).

In Subsection III B, we demonstrated that interrupted coarsening occurs in the solutions of the one-dimensional EOM (5). Our simulations in two dimensions also exhibit interrupted coarsening. Evidence for this is seen in Fig. 15, which is a plot of the surface width (i.e., the standard deviation of the surface height) versus time for the simulation that produced the surface seen in Fig. 9. The surface width grows for some time and then appears to asymptote to a finite value. Furthermore, inspection of Fig. 9 itself shows that both the lateral and

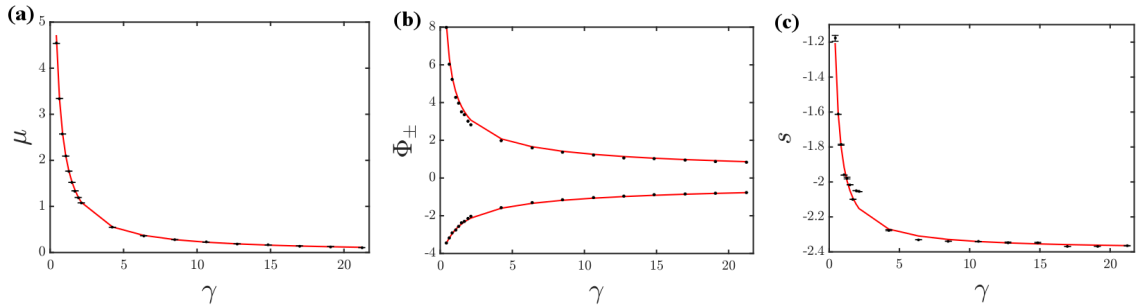

FIG. 14: (Color online) (a) Downward drift speeds μ, (b) selected slopes $\Phi_\pm$ and (c) propagation velocities s. The data points are values obtained from simulations of Eq. (2). The red curves are predictions from the 1D theory: (a) μ as given by Eq. (25), (b) $\Phi_\pm$ as given by Eq. (7) and (c) s as given by Eq. (9). The surfaces were simulated to time $t = 500$ and the parameter values used were $\kappa_1 = -0.5$, $\kappa_2 = 10$, $\lambda_1 = -0.5$, $\lambda_2 = -0.5$ and $\gamma_2 = 0$.

vertical scales of the surface grow from (a) to (b) but are not substantially changed from (b) to (c). We observed interrupted coarsening in all of our simulations in 2D.

D. Elongated pyramidal structures

Next we present simulation results which resemble a specific topography seen in experiments performed by Carter *et al.* at high angles of incidence [8]. Both the experimental surfaces and our simulated surfaces exhibit pyramidal structures which protrude from the surface and that are elongated in the projected ion beam direction. We see these structures form in our numerical integrations of Eq. (2) when there is a linear instability in the transverse direction (i.e., $\kappa_2 < 0$) and the magnitudes of both γ_1 and γ_2 are sufficiently large. Since the pyramidal structures only form in simulations with nonzero values of γ_2, the term $u_x u_y^2$ plays an critical role in their formation. One such simulation result is shown in Fig. 16. Notice that the pyramidal structures that form in our simulation have ends that tend to line up, just as in the experiments described in Ref. [8]. The gradient distribution for Fig. 16 is shown in Fig. 17. Clearly, there is a strongly selected negative value of u_x in this simulation. Furthermore, the gradient distribution demonstrates that the elongated portion of the pyramidal structures have $u_x > 0$ and the ends of the elongated pyramids have $u_x < 0$; i.e., these pyramidal structures protrude from the surface with their ends facing the ion source. This is again consistent with Carter *et al.'s* experimental observations. The

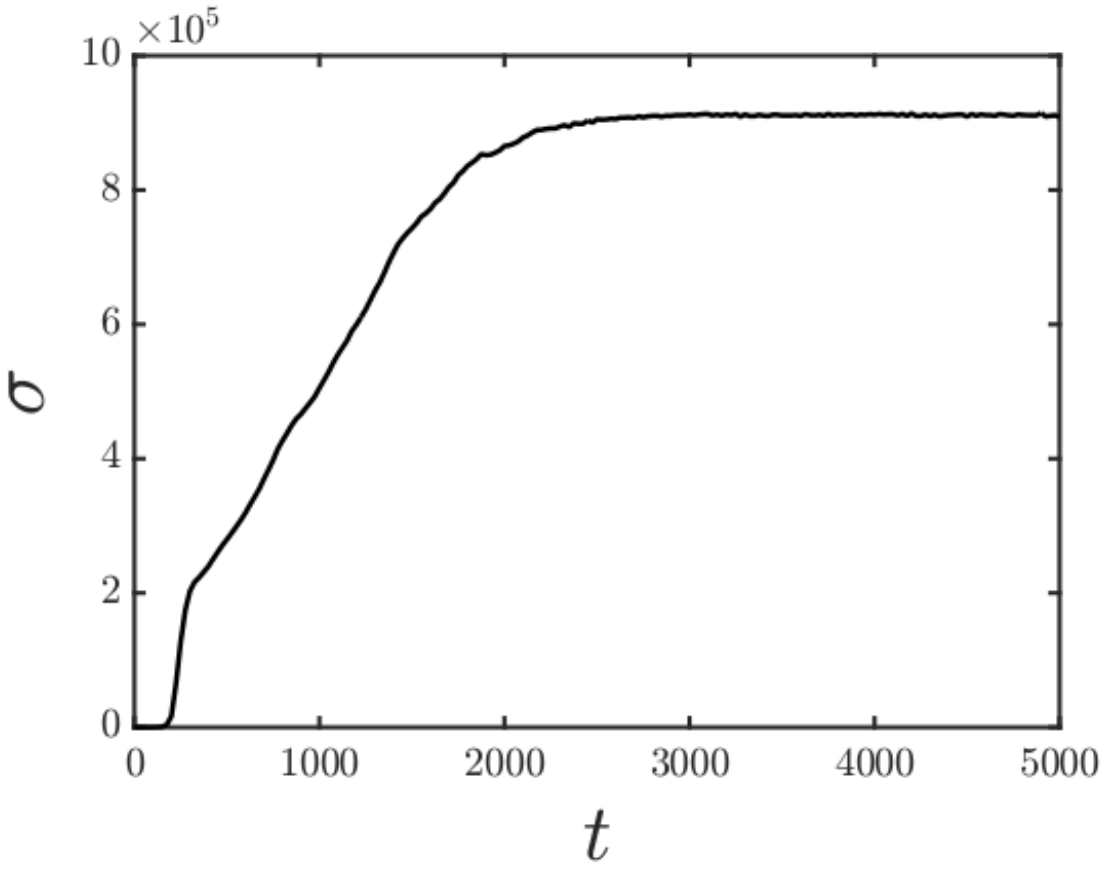

FIG. 15: The surface width versus time obtained from a simulation of Eq. (2). The figure shown is produced from the same simulation that yielded Fig. 9.

mean curvature of the surface — which is shown in Fig. 18 — shows that shocks which are elongated in the longitudinal direction can form. These shocks are close to being aligned with the x-axis but are not parallel to it. To see this, note that if we consider a surface which has no longitudinal variations, then Eq. (2) reduces to

$$u_t = \kappa_2 u_{yy} - B u_{yyyy} + \lambda_2 u_y^2. \tag{26}$$

This is the KS equation and it does not lead to shock formation.

In the simulation we just discussed, perpendicular-mode ripples formed at early times. However, elongated pyramidal structures can also form when parallel-mode ripples are present for low fluences. Figure 19 demonstrates this with two snapshots of a surface obtained by simulating Eq. (2): (a) shows the surface at time $t = 150$ and (b) shows the same surface at a later time ($t = 850$). Our simulation results are remarkably similar to the topographies obtained by Datta *et al.* when they irradiated a germanium surface with 100

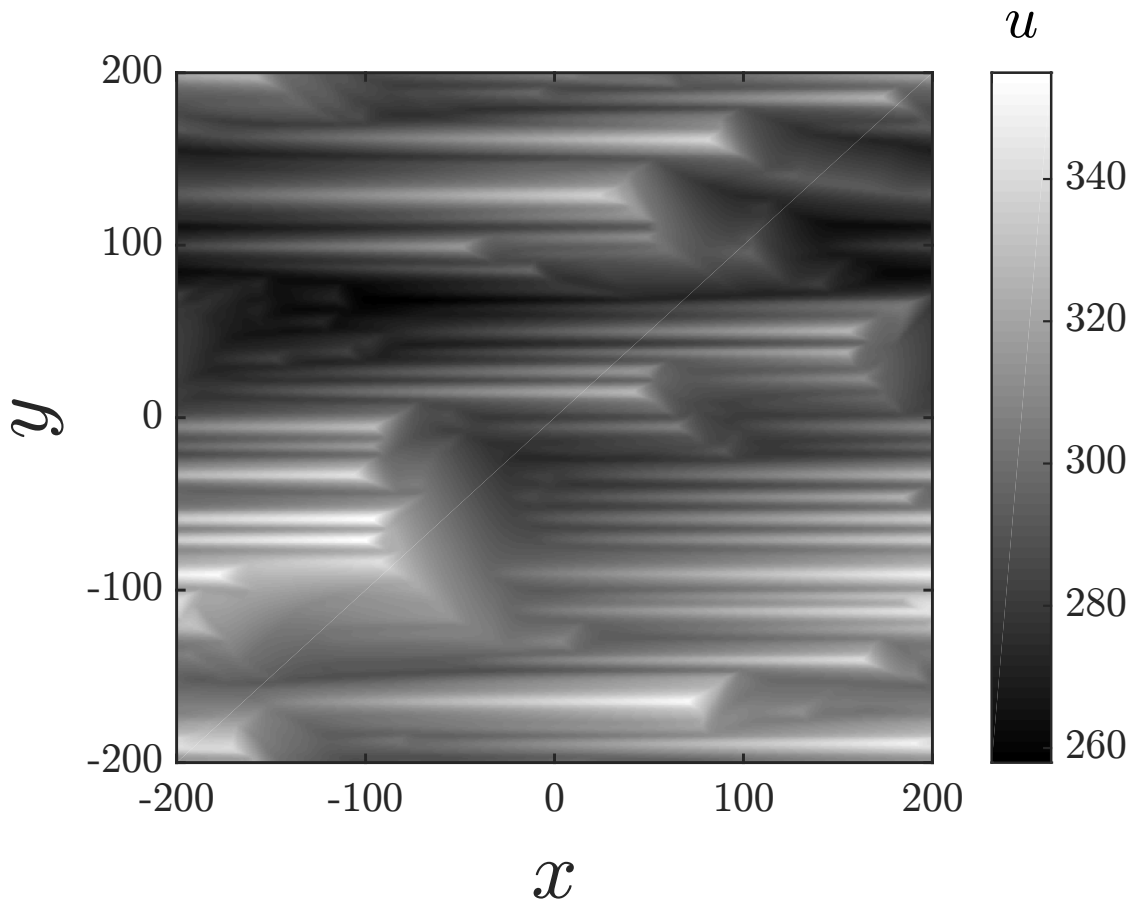

FIG. 16: A surface obtained by integrating Eq. (2) up to time $t = 1800$, starting from a low amplitude white noise initial condition. At early times, perpendicular-mode ripples formed. Later, these ripples evolved into the elongated pyramidal structures seen in the figure. The parameter values used were $\kappa_1 = 0$, $\kappa_2 = -0.6$, $B = 1$, $\lambda_1 = 0.5$, $\lambda_2 = 0.5$, $\gamma_1 = 1$ and $\gamma_2 = -3$.

keV krypton ions at a 60° angle of incidence: see Fig. 3 of Ref. [20]. Datta *et al.* found that the parallel-mode ripples that developed at early times ultimately evolved into elongated pyramidal structures, just as in our simulations.

E. Lenticular Depressions

Lenticular depressions are another interesting topographical feature that have been observed in experiments. These lens-shaped depressions are prominent, for instance, in Fig. 3 (f) of Ref. [18], in which silicon was bombarded with a 1.2 keV xenon ion beam with a 75°

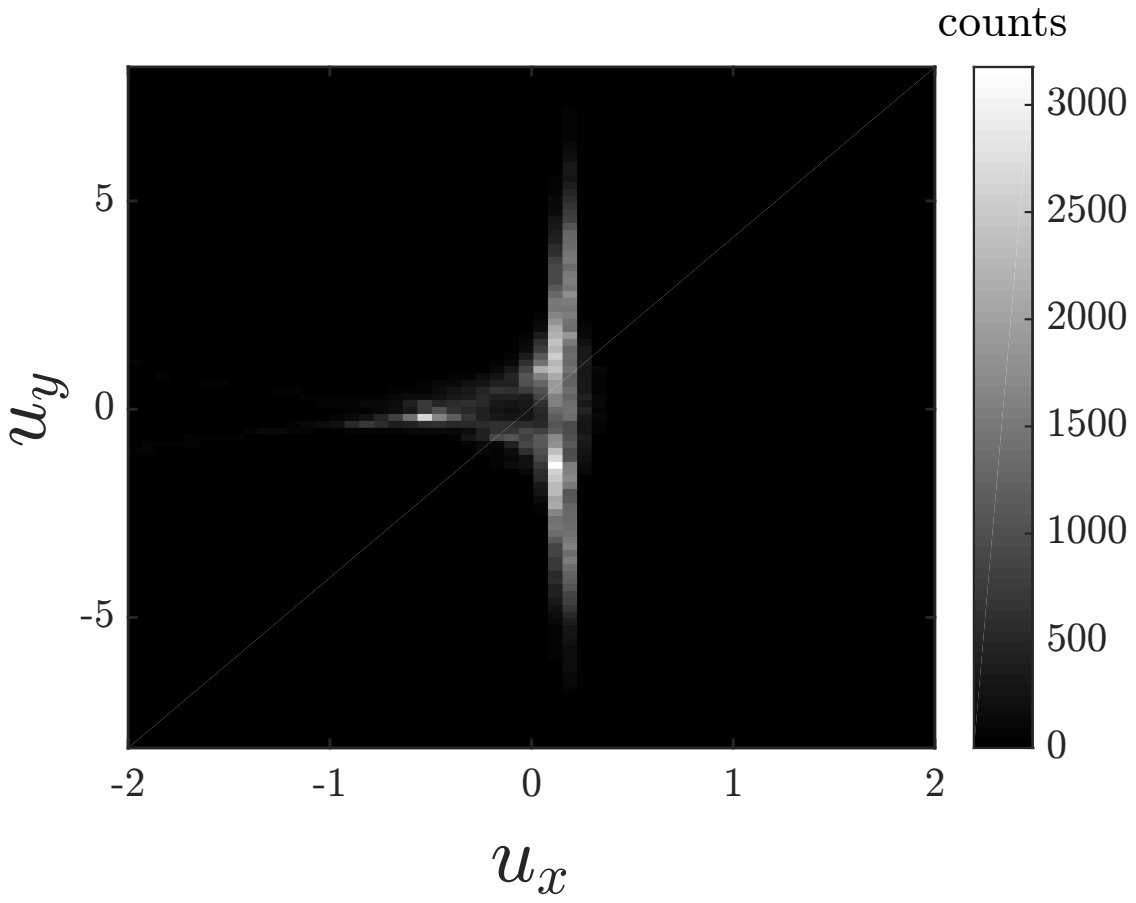

FIG. 17: The gradient distribution of the surface obtained from a simulation of Eq. (2), integrated up to time $t = 1800$. The figure was obtained from the surface seen in Fig. 16.

angle of incidence. We have also seen lenticular depressions in some simulations of Eq. (2) in which the initial condition was low amplitude spatial white noise — see Fig. 20 (a) for an example. The mean curvature of that surface is shown in Fig. 20 (b). This figure shows that the pit's edge is a shock and there is a complicated cellular structure outside of the pit. There is also a shock that crosses the bottom of the pit. In the experiments, the outlines of the lenticular depressions appear to be shocks and shocks traverse the base of the pits, just as in our simulations.

Lenticular features arise in our simulations if the value of γ_1 is slightly larger than the threshold value for terrace formation. They are transient structures which appear when the surface is transitioning from KS-like behavior to a terraced topography. In fact, in this simulation, the emergence of the depression corresponds to the emergence of the first undercompressive shock. Since $\gamma_2 = 0$ in the simulation that produced Fig. 20, it is clear

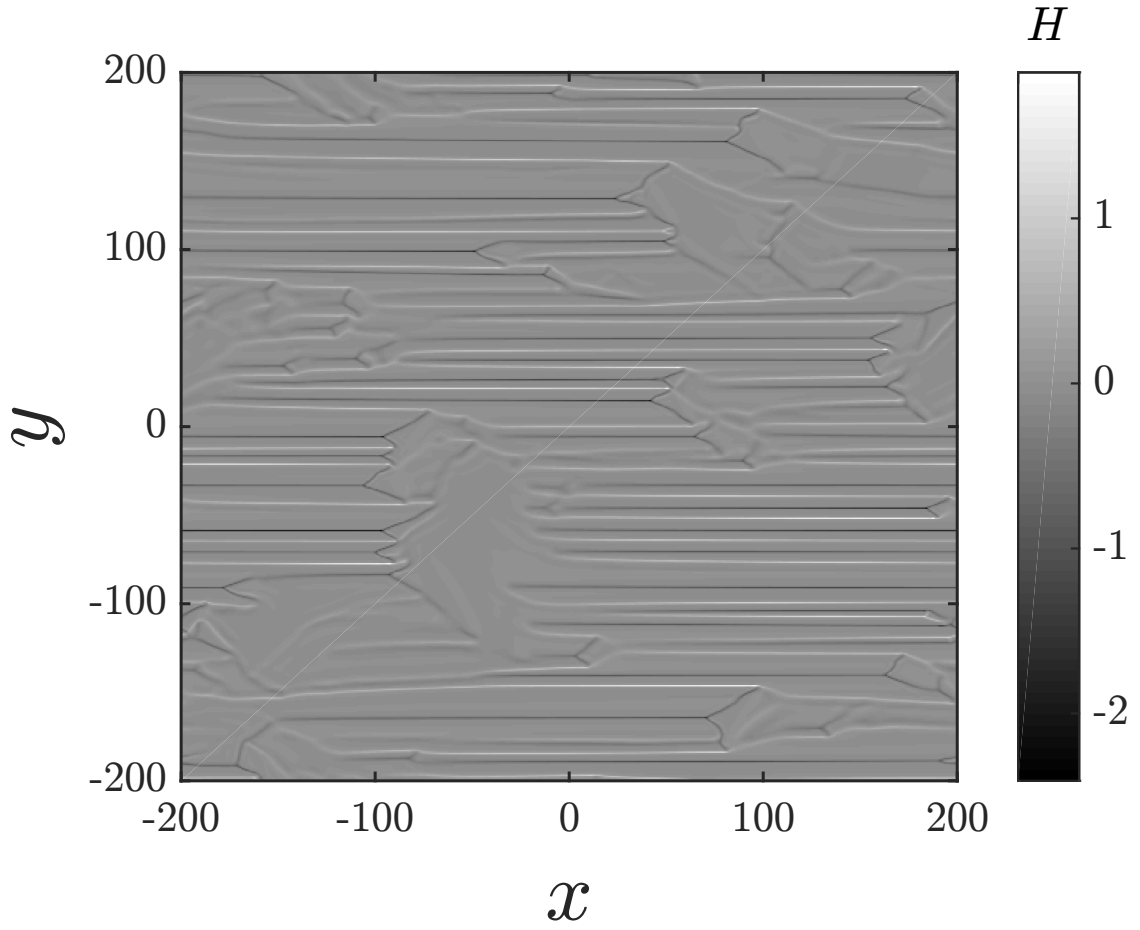

FIG. 18: The mean curvature H of the surface shown in Fig. 16. Shocks that are elongated in the longitudinal direction are evident.

that the term $u_x u_y^2$ is not necessary for the formation of lenticular depressions. However, its inclusion can modify their shape.

V. CONCLUSIONS

In this paper, we analyzed the solutions to the PB equation (5), the equation of motion that governs the formation of terraced structures on solid surfaces that are bombarded with a broad ion beam with a high angle of incidence when the surface height does not depend on the transverse coordinate y. Our work builds upon Ref. [21], in which Eq. (5) was first studied in this context.

We found that between the undercompressive shocks where the surface slope changes rapidly, the terraced surfaces are not perfectly flat, but instead develop small scale ripples

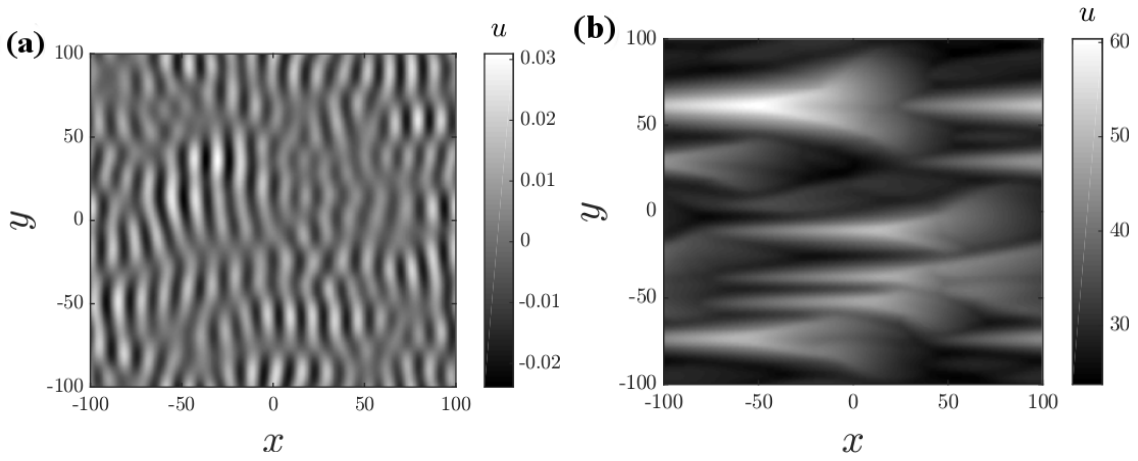

FIG. 19: (a) A surface obtained by integrating Eq. (2) up to time $t = 150$, starting from a low amplitude white noise initial condition. Parallel-mode ripples are evident. (b) At time $t = 850$, the surface exhibits elongated pyramidal structures. The parameter values used in this siumulation were $\kappa_1 = -0.5$, $\kappa_2 = -0.3$, $B = 1$, $\lambda_1 = -0.05$, $\lambda_2 = -0.5$, $\gamma_1 = 1$ and $\gamma_2 = -3$.

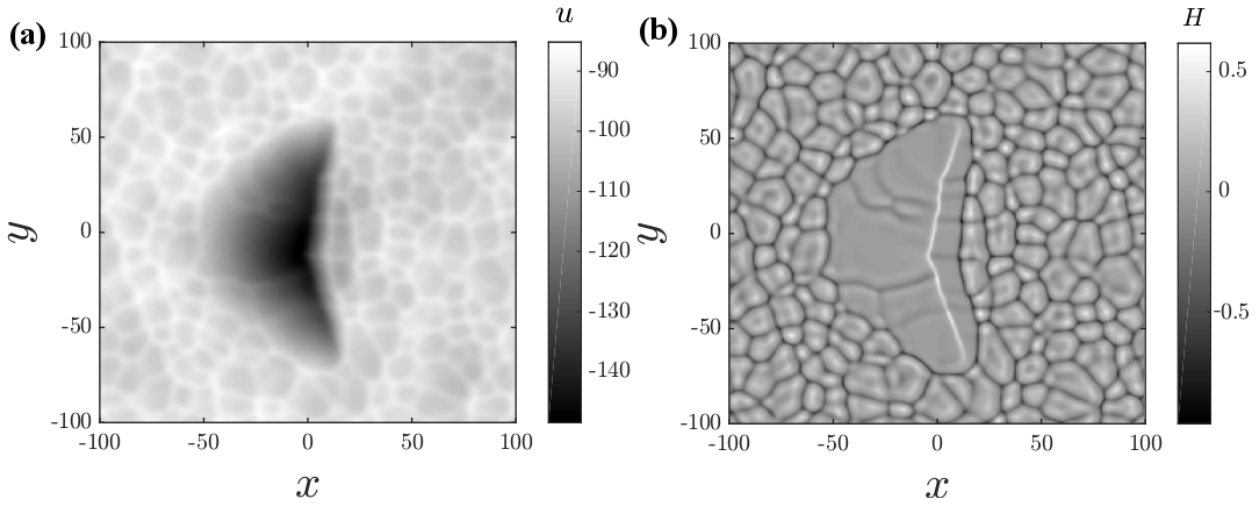

FIG. 20: (a) A surface obtained by integrating Eq. (2) up to time $t = 465$, starting from a low amplitude spatial white noise initial condition. A lenticular depression is shown, surrounded by a region of the surface which looks very much like what would be seen in simulations of the isotropic KS equation. (b) The mean curvature H of the surface in (a). The parameters were $\kappa_1 = -0.5$, $\kappa_2 = -0.5$, $B = 1$, $\lambda_1 = -0.5$, $\lambda_2 = -0.5$, $\gamma_1 = 0.11$ and $\gamma_2 = 0$.

which propagate along the surface. Our analysis predicts the amplitude and propagation velocity of these ripples. The accuracy of these predictions was confirmed by numerical simulations. We also presented numerical evidence that shows that solutions to the PB equation exhibit interrupted coarsening, i.e., the lateral length scale and characteristic amplitude of the solutions grow for a time, and then asymptote to finite values. The characteristic length scale of the solutions to Eq. (5) in the long-time limit was shown to not depend on the size of the sample considered.

The one free parameter in the PB equation (γ) is a dimensionless measure of the strength of the cubic nonlinearity. From the results of extensive numerical simulations, we were able to identify a critical value of this parameter: $\gamma_c \simeq 0.277$. For γ greater than γ_c, the surface becomes fully terraced at sufficiently long times. The time T_{tf} needed for solutions to the PB equation (5) to reach a well formed terraced state diverges rapidly as γ tends to γ_c from above. Conversely, no terrace formation was observed in simulations with γ values below γ_c; instead, the solutions appear to display the spatiotemporal chaos that is characteristic of the Kuramoto-Sivashinsky equation, the equation that is obtained in the $\gamma \to 0$ limit.

The parameter γ depends on the angle of ion incidence θ. It is expected to increase from small to rather large values as θ is increased through a range of values [21]. Thus, γ should pass through the critical value γ_c as the angle of incidence increases. If this indeed occurs, our theory predicts that as θ is increased, the surface morphology at a given ion fluence will undergo a transition from an unterraced to a terraced state. There is already indirect experimental evidence that such a transition does in fact occur, since terraced morphologies have only been observed at relatively high angles of incidence [7–20]. Systematic experiments in which θ is increased for a given choice of target material and of ion species and energy would be a valuable test of our theory.

We also studied an equation of motion that generalizes the PB equation to the case in which the surface height depends on both the longitudinal and transverse coordinates. This equation differs from the usual equation of motion (the anisotropic two-dimensional Kuramoto-Sivashinsky equation) by the inclusion of the cubic nonlinearities u_x^3 and $u_x u_y^2$. Although it is not the most general equation of motion that includes terms up to cubic order in u, the generalized PB equation captures many of the features that are observed in experiments in which the angle of ion incidence is relatively high. For example, for a range of parameter values, it yields parallel-mode ripples at early times. These ripples then evolve

into a terraced structure which coarsens with time. For other ranges of the parameters, the surface develops other morphologies reminiscent of those seen in experiments, such as isolated lenticular depressions and elongated pyramidal structures that tilt up out of the surface and towards the beam.

The strong similarities between the surfaces produced by our model and those observed in experiments indicates that the cubic nonlinearities u_x^3 and $u_x u_y^2$ play a crucial role in the dynamics for sufficiently high angles of ion incidence. These nonlinearities could be eliminated in an experiment by bombarding the surface with identical, diametrically opposed beams, or by periodically and rapidly rotating the sample through 180° increments about its surface normal. In experiments of this kind, the equation of motion is invariant under the transformation $x \to -x$ and the morphologies produced should differ markedly from those that develop when the sample is stationary and a single, near glancing incidence ion beam is employed.

Acknowledgments

We would like to thank Mark Hoefer, Greg Lyng, Carmen Menoni, Matt Pennybacker, Emmett Randel and Patrick Shipman for valuable discussions. R.M.B. is grateful to the National Science Foundation for its support through grant DMR-1508745.

[1] J. Muñoz-García, L. Vázquez, M. Castro, R. Gago, A. Redondo-Cubero, A. Moreno-Barrado and R. Cuerno, *Mater. Sci. Eng. R-Rep.* **86**, 1 (2014).

[2] P. Sigmund, *J. Mater. Sci.* **8**, 1545 - 1553 (1973).

[3] R. M. Bradley and J. M. E. Harper, *J. Vac. Sci. Technol. A* **6**, 2390 - 2395 (1988).

[4] G. Carter and V. Vishnyakov, *Phys. Rev. B* **54**, 17647 - 17653 (1996).

[5] R. Cuerno and A.-L. Barabási, *Phys. Rev. Lett.* **74**, 4746 - 4749 (1995).

[6] M. A. Makeev, R. Cuerno and A.-L. Barabási, *Nucl. Instrum. Methods Phys. Res., Sect. B* **197**, 185 - 227 (2002).

[7] W. Hauffe, *Phys. Stat. Sol. A* **35**, K93 - K96 (1976).

[8] G. Carter, M. J. Nobes, F. Paton, J. S. Williams and J. L. Whitton, *Radiation Effects and Defects in Solids* **33**, 65 - 73 (1977).

[9] D. Flamm, F. Frost and D. Hirsch, *Appl. Surf. Sci.* **179**, 96 - 101 (2001).

[10] D. P. Datta and T. K. Chini, *Phys. Rev. B* **69**, 235313 (2004).

[11] P. Karmakar and D. Ghose, *Nucl. Inst. Meth. Phys. Res. B* **230**, 539 - 544 (2005).

[12] D. P. Adams, T. M. Mayer, M. J. Vasile and K. Archuleta, *Appl. Surf. Sci.* **252**, 2432 - 2444 (2006).

[13] Q. Wei, J. Lian, L. A. Boatner, L. M. Wang and R. C. Ewing, *Phys. Rev. B* **80** 085413 (2009).

[14] P. Mishra and D. Ghose, *J. Appl. Phys.* **105**, 014304 (2009).

[15] A. Metya, D. Ghose, S. A. Mollick and A. Majumdar, *J. Appl. Phys.* **111**, 074306 (2012).

[16] T. Basu, J. R. Mohanty, and T. Som, *Appl. Surf. Sci.* **258**, 9944 (2012).

[17] T. Basu, D. P. Datta and T. Som, *Nanoscale Res. Lett.* **8**, 289 (2013).

[18] M. Teichmann, J. Lorbeer, B. Ziberi, F. Frost and B. Rauschenbach, *New J. Phys.* **15**, 103029 (2013).

[19] M. Engler, S. Macko, F. Frost and T. Michely, *Phys. Rev. B* **89**, 245412 (2014).

[20] D. P. Datta, S. K. Garg, T. Basu, B. Satpati, H. Höfsass, D. Kanjilal and T. Som, *Appl. Surf. Sci.* **360**, 131 (2016).

[21] D. A. Pearson and R. M. Bradley, *J. Phys.: Cond. Matt.* **27**, 015010 (2015).

[22] Undercompressive shocks had been encountered previously in studies of ion sputtering: see H. H. Chen, O. A. Urquidez, S. Ichim, L. H. Rodriquez, M. P. Brenner, and M. J. Aziz, *Science*

310, 294 - 297 (2005); M. Holmes-Cerfon, W. Zhou, A. L. Bertozzi, M. P. Brenner and M. J. Aziz, *Appl. Phys. Lett.* **101**, 143109 (2012); and M. Holmes-Cerfon, M. J. Aziz and M. P. Brenner, *Phys. Rev. B* **85**, 165441 (2012).

[23] M. P. Harrison and R. M. Bradley, *J. Appl. Phys.* **121**, 054308 (2017).

[24] M. P. Harrison and R. M. Bradley, *J. Appl. Phys.* **121**, 225304 (2017).

[25] M. Rost and J. Krug, *Phys. Rev. Lett.* **75**, 3894 (1995).

[26] M. Moseler, P. Gumbsch, C. Casiraghi, A. C. Ferrari, and J. Robertson, Science **309**, 1545 (2005).

[27] B. Davidovitch, M. J. Aziz, and M. P. Brenner, Phys. Rev. B **76**, 205420 (2007).

[28] C. C. Umbach, R. L. Headrick, and K.-C. Chang, Phys. Rev. Lett. **87**, 246104 (2001).

[29] R. M. Bradley and H. Hofsäss, J. Appl. Phys. **120**, 074302 (2016).

[30] H. Hofsäss, K. Zhang and O. Bobes, J. Appl. Phys. **120**, 135308 (2016).

[31] T. Kawahara, *Phys. Rev. Lett.* **51**, 381 (1983).

[32] M. P. Gelfand and R. M. Bradley, *Phys. Lett. A* **379**, 199 (2015).

[33] M. Castro, R. Cuerno, L. Vázquez and R. Gago, *Phys. Rev. Lett.* **94**, 016102 (2005).

[34] J. Muñoz-García, M. Castro and R. Cuerno, *Phys. Rev. Lett.* **96**, 086101 (2006).

[35] J. Muñoz-García, R. Cuerno and M. Castro, *Phys. Rev. B* **78**, 205408 (2008).

[36] S. M. Cox and P. C. Matthews, *J. Comput. Phys.* **176**, 430 (2002).

[37] A.-K. Kassam and L. N. Trefethen, *SIAM J. Sci. Comput.* **26**, 1214 (2005).